Tailoring sample-wide pseudo-magnetic fields on a graphene–black phosphorus heterostructure

Yanpeng Liu [1,2], J. N. B. Rodrigues[2,3], Yong Zheng Luo [3], Linjun Li[1,2], Alexandra Carvalho[2,3], Ming Yang[2,3,4], Evan Laksono[2,3], Junpeng Lu[2,3], Yang Bao [1,2], Hai Xu[1,2], Sherman J. R. Tan [5], Zhizhan Qiu[5], Chorng Haur Sow[2,3], Yuan Ping Feng [2,3], A. H. Castro Neto [2,3], Shaffique Adam [2,3,6]*, Jiong Lu[1,2]* and Kian Ping Loh[1,2]*

Spatially tailored pseudo-magnetic fields (PMFs) can give rise to pseudo-Landau levels and the valley Hall effect in graphene. At an experimental level, it is highly challenging to create the specific strain texture that can generate PMFs over large areas. Here, we report that superposing graphene on multilayer black phosphorus creates shear-strained superlattices that generate a PMF over an entire graphene–black phosphorus heterostructure with edge size of tens of micrometres. The PMF is intertwined with the spatial period of the moiré pattern, and its spatial distribution and intensity can be modified by changing the relative orientation of the two materials. We show that the emerging pseudo-Landau levels influence the transport properties of graphene–black phosphorus field-effect transistor devices with Hall bar geometry. The application of an external magnetic field allows us to enhance or reduce the effective field depending on the valley polarization with the prospect of developing a valley filter.

Due to the combination of its massless Dirac fermion-like band structure and its lattice symmetry (C_{3v}), the electronic properties of graphene are easily influenced by mechanical deformations, thus providing a means to tune carrier dynamics in graphene with strain[1,2]. A non-uniform strain affects the two sublattices of bipartite graphene differently, and shifts the Dirac cones in opposite directions, creating pseudo-magnetic fields (PMFs)[3–6]. The existence of a PMF is of profound interest because it generates an energy gap and leads to a zero-magnetic-field analogue of the quantum Hall effect[5]. Nevertheless, there is no practical means yet discovered to control the spatial distribution or intensity of this strain-related PMF. Theoretical studies have predicted that a strain field with threefold symmetry can induce PMFs in graphene, but the technique to implement such a strain field has not been developed[3,5–7]. So far, non-planar deformations such as bubbles or ripples have facilitated the observation of giant local PMFs using scanning tunnelling microscopy (STM), but the influence of PMFs on the transport properties of graphene over a mesoscopic scale has not been studied[8,9].

In this study, using STM we discover that when hexagonal graphene is interfaced with orthorhombic black phosphorus (BP), both lattices are mutually strained and sheared, giving rise to a periodically fluctuating PMF. It is well known that, due to the elastic properties of graphene, strained superlattices can be created when graphene is stacked on a lattice-mismatched substrate[10–12]. In contrast to heterostructures made from graphene and hexagonal boron nitride, where the constituent layers share the same lattice symmetry with a slight lattice mismatch, a non-hexagonal substrate with large lattice mismatch can impose a more complex strain texture encompassing a combination of strain, shear or twist on graphene[11–14].

We also find that by simply changing the rotation angle between the graphene and BP, the intensity and spatial distribution of the PMFs on the graphene can be tuned.

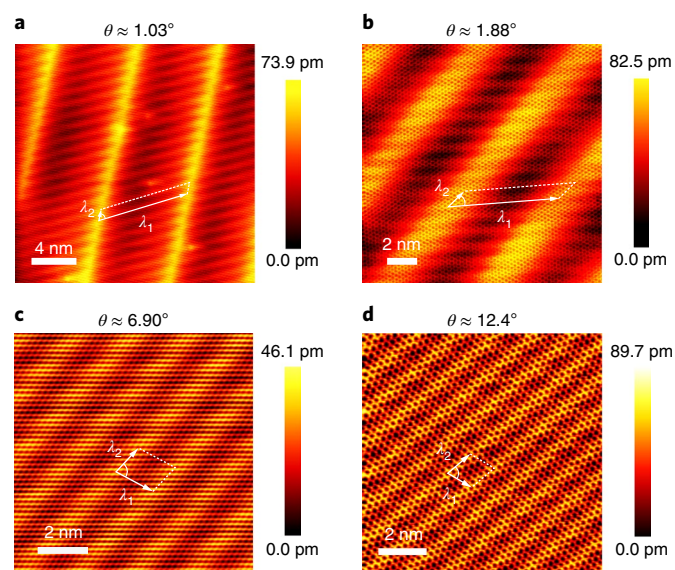## Rotation-angle-dependent moiré superlattices

To fabricate a graphene-on-BP heterostructure (G–BP), monolayer graphene was transferred onto a multilayer BP flake (Fig. 1a) using standard transfer techniques, followed by annealing in ultrahigh vacuum ($<1 \times 10^{-10}$ torr) to ensure conformal contact at the interface (see Methods)[11,15]. The puckered honeycomb structure of BP significantly reduces its rigidity, so a thicker BP ($h \geq 4.0$ nm) was used to ensure that the BP layer induced strain on the graphene[16–18]. For the G–BP heterostructure, rotation angle θ is defined as the small angle between the zigzag direction of the BP and one zigzag direction of the graphene (Fig. 1b), which were determined using polarized Raman spectroscopy (see Methods)[15,19]. The superposition of hexagonal graphene and orthorhombic BP lattices leads to different interference patterns related to both the lattice mismatch δ and rotation angle θ.

The θ dependence of the moiré superlattices in the G–BP system was investigated using STM. A diversity of moiré patterns was generated by varying the rotation angles, as shown in Fig. 2. Due to interference between the unit cell vectors of graphene with two different BP crystallographic vectors in its orthorhombic lattice, two moiré superlattices are produced, characterized by a θ-dependent large moiré wavelength (λ_1), which varies in the range ~8.0–0.77 nm, and a smaller moiré superlattice with a wavelength (λ_2) that varies between ~0.89 and 1.32 nm (see Supplementary Fig. 1 for more examples of θ). Similar to the formation of beats when two sound waves of slightly different frequencies are superimposed, beats in the form of

[1]Department of Chemistry, National University of Singapore, Singapore, Singapore. [2]Centre for Advanced 2D Materials and Graphene Research Centre, National University of Singapore, Singapore, Singapore. [3]Department of Physics, National University of Singapore, Singapore, Singapore. [4]Institute of Materials Research and Engineering, Agency for Science, Technology and Research, Singapore, Singapore. [5]NUS Graduate School for Integrative Sciences and Engineering, National University of Singapore, Singapore, Singapore. [6]Yale-NUS College, Singapore, Singapore. *e-mail: shaffique.adam@yale-nus.edu.sg; chmluj@nus.edu.sg; chmlohkp@nus.edu.sg
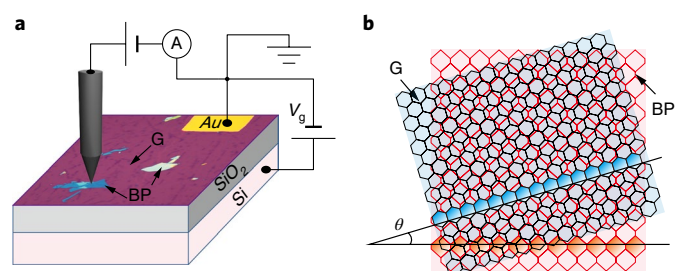
Fig. 1 | Schematic of G–BP device. a, Schematic of the measurement set-up showing the STM tip and including an optical image (dimension: ~150 μm × ~200 μm) of one of the samples. G and BP represent monolayer graphene and the multilayer black phosphorus flake, SiO_2 is 300-nm-thick silicon dioxide, Si is highly doped silicon and A is the set tunnelling current. The graphene is grounded via a gold electrode (sketched). Note that the gold pad is at millimetre distances away from the G–BP sample in the actual device geometry. A back-gate voltage V_g is applied through the doped Si electrode. **b**, Sketch of graphene on BP showing the emergence of moiré patterns. Rotation angle θ is defined as the angle between the BP zigzag direction and the nearest graphene zigzag direction.

where b_1 and b_2 ($b_1 < b_2$) are BP lattice constants, and δ_i are the mismatch with the redefined graphene lattice vectors ($\delta_1 = \frac{b_1}{a} - 1 \approx 0.34$ and $\delta_2 = \frac{b_2}{a\sqrt{3}} - 1 \approx 0.02$; a is the lattice constant of graphene). Consistent with the experimental observations, we found that the short moiré period (~1 nm) depends only weakly on the angle due to the larger δ_1, while the long moiré period changes between ~8.0 nm and ~0.8 nm depending on the orientation angle. Our simulations also show that to account for the experimentally observed large and small moiré periods, the corresponding graphene lattices need to be strained. Figure 3a shows a simulated moiré superlattice at $\theta \approx 1.03°$ along with strained lattices of both graphene and BP. This reproduces the stripe-like pseudo-1D moiré pattern observed by STM (Fig. 2a); the agreement is also good for other rotation angles (Supplementary Fig. 3).

Angle-dependent strain and pseudo-magnetic fields

From the STM topography image (Fig. 2a, $\theta \approx 1.03°$), the local displacement of each unit cell can be calculated by identifying the coordinate of each graphene unit cell (for detailed calculations see Supplementary Note 4 and Supplementary Fig. 4), from which the corresponding strain tensors and PMFs are derived (PMFs: $B_s =$

Fig. 2 | Angle-dependent moiré superlattices. a–d, STM topography images showing the coexistence and evolution of two sets of moiré superlattices (λ_1 and λ_2 represent the wavelengths of a large and small moiré superlattice. Tunnelling parameters: $V_s = 0.4$ V, $I = 0.8$ nA (**a**); $V_s = -0.75$ V, $I = 0.8$ nA (**b**); $V_s = -0.35$ V, $I = 1.0$ nA (**c**); $V_s = 0.08$ V, $I = 0.5$ nA (**d**); $\lambda_1 \approx 7.8$ nm (**a**); 7.13 nm (**b**); 1.69 nm (**c**); 1.15 nm (**d**). For more moiré superlattices see Supplementary Fig. 1 (for $\theta \approx 2.8°$, 5.6°, 5.9°, 8.9°, 10.5°, 15.7°).

a pseudo-one-dimensional (pseudo-1D) striped diagonal pattern are produced because of the interference of these superlattices.

To reproduce the moiré patterns observed in STM, we simulated the rotation of a graphene monolayer on BP using a geometrical model (for more calculation details see Supplementary Note 2 and Supplementary Fig. 2). The two moiré periods are defined as
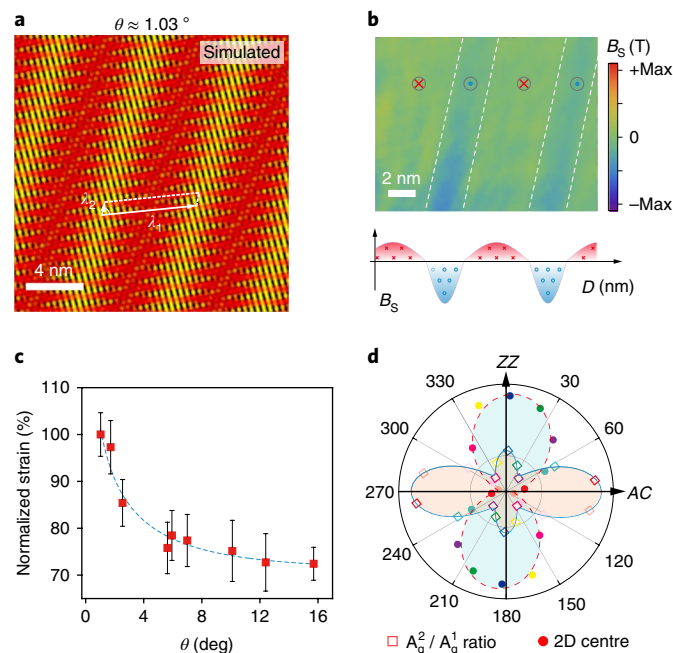
$$\lambda_1 = \frac{b_2}{\sqrt{\delta_2^2 + 2(1+\delta_2)(1-\cos\theta)}}$$

$$\lambda_2 = \frac{b_1}{\sqrt{\delta_1^2 + 2(1+\delta_1)(1-\cos\theta)}}$$

(1)

Fig. 3 | Spatial pseudo-magnetic field texture and θ-dependent strain. a, Theoretically derived moiré superlattice showing lattice constants (g_i) of graphene along the three zigzag directions $g_1 = 2.37$ Å, $g_2 = 2.44$ Å and $g_3 = 2.49$ Å, while BP is strained by 0.6% and 5.0% along its zigzag and armchair directions, respectively. **b**, Texture of the PMF generated within graphene for rotation angle $\theta \approx 1.03°$. Bottom, schematic showing the spatially alternating distribution. **c**, Plot of calculated biaxial strain levels against rotation angle θ, taking shear strain into account. In our experiments, the smallest observed rotation angle is $\theta \approx 1.03°$. We thus normalized the strain eigenvalues with respect to the strain values under this angle. The blue dashed line is the non-linear fitting of the experimental data plots. Error bars indicate standard deviation (s.d.) of normalized strain due to different sets of unit vectors at each angle. **d**, Angle-resolved Raman mapping of A_g^2/A_g^1 ratios of BP (open symbols are measured values; blue line the theoretical fit; the intensity ratio of A_g^2/A_g^1 reaches a maximum when the excitation laser is polarized along the armchair direction of the BP crystal) and 2D peak positions of graphene (solid symbols are experimental 2D positions; red dashed line is fitted curve).
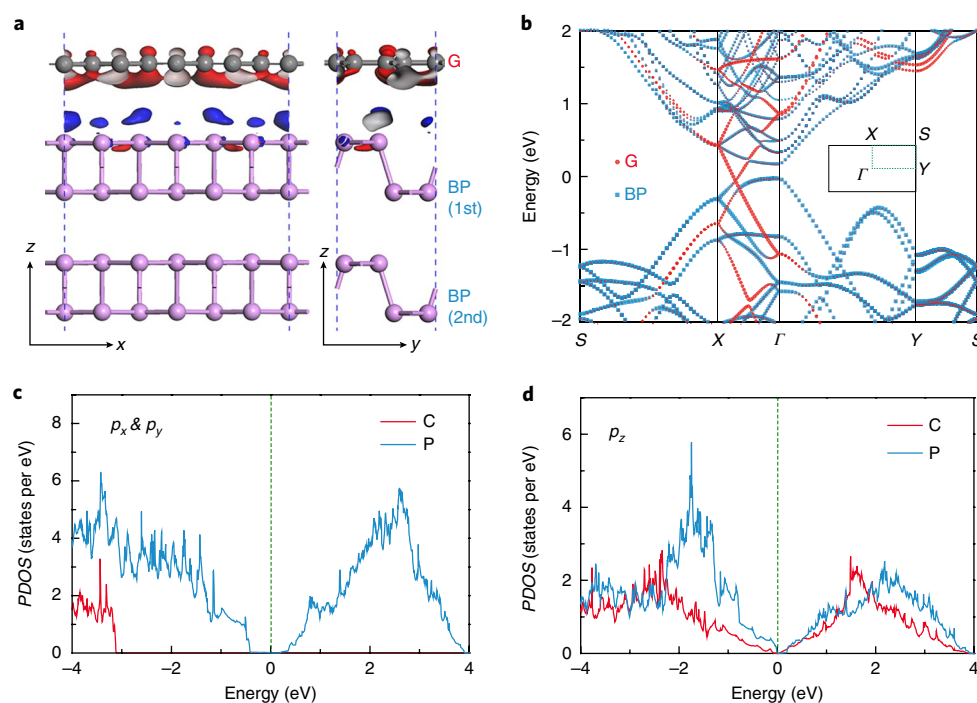
Fig. 4 | Structural and electronic properties of G–BP heterostructure. a, Front view (left) and side view (right) of optimized graphene (G) on bilayer black phosphorus (BP). The superimposed differential charge density is visualized by an iso-surface value of 5.0×1.0^{-5} e Å^{-1}, and the red and blue colours denote the depleted and accumulated charge density, respectively. **b**, Projected band structure of the graphene on bilayer black phosphorus, in which the red dots and blue square lattices denote the contribution of graphene and black phosphorus, respectively. **c,d**, Projected $p_x \& p_y$ and p_z density of states (PDOS) for the graphene on bilayer black phosphorus. C and P in **c** and **d** represent carbon and phosphorus atoms. The Fermi level is fixed at 0 eV.

$\nabla \times \mathbf{A}$, where $\mathbf{A}$ is the pseudo-vector potential). From these data, we have computed the spatial distribution of PMFs arising from elastic lattice deformations using the low-energy effective model for graphene (the massless Dirac Hamiltonian: $H = \nu_F \tau_z \otimes \boldsymbol{\sigma} \cdot \left(\mathbf{p} + \frac{e}{\hbar} \mathbf{A} \right)$, where ν_F is the Fermi velocity, $\mathbf{p}$ is the momentum operator, $\boldsymbol{\sigma} = (\sigma_x, \sigma_y)$, and σ_i and τ_i are the Pauli matrices acting, respectively, on the pseudo-spin and valley quantum numbers)[3,4,20]. As shown in Fig. 3b, the calculated PMF texture shows a moiré-modulated strip with alternating negative and positive PMF distribution. Such a behaviour is similar to counter-propagating cyclotron orbits in valleys with opposite pseudo-spins, as demanded by time-reversal symmetry. The relation between the period of the oscillating PMFs with the strip-like diagonal moiré pattern suggests that it is possible to engineer the intensity and distribution of PMFs by altering the moiré pattern, which is achieved by simply changing the angle of rotation. For example, by increasing θ to ~12.4°, we can reduce the width of the stripe-like moiré pattern to ~1.0 nm (Supplementary Fig. 7).

Because non-uniform strain is understood to be the origin of PMFs, it is necessary to analyse the nature of strain on the graphene and BP layers by analysing the moiré pattern in detail. In contrast to the direct space (topography image), lattice constants, rotation angles and moiré wavelengths are more accurately determined in the reciprocal space (for fast Fourier transform (FFT) of topography images, see Supplementary Fig. 8)[21]. First, the presence of shear strain is clearly indicated by the observation that the spots originating from graphene are not commensurate with the extrapolated reciprocal space lattice vectors. Second, we find that the BP layer in contact with graphene is also strained along both its zigzag and armchair directions (more FFTs and distorted P atoms position maps are provided in Supplementary Fig. 9).

To better analyse the different components of the strain in the G–BP system, we separate the contribution of shear strain into three components: (1) isotropic rescaling (p_{iso}) corresponding to biaxial strain; (2) anisotropic rescaling (p_{an}, at angle φ_1); (3) an additional rotation (at angle φ_2). By doing this, we have qualitatively estimated

the variation of the overall in-plane strain as function of θ from an extension of Hermann's formalism for the G–BP system (for more calculation details see Supplementary Note 8)[21]. Using experimentally observed parameters for each θ (directly read from each FFT of topography images in Fig. 2 and Supplementary Fig. 1), a plot of the average biaxial strain versus rotation angle θ is shown in Fig. 3c. It is seen that the strain on graphene decreases monotonically with increasing θ. In other words, the highest strain is observed when the zigzag direction of graphene is aligned with the zigzag direction of BP. The generated in-plane strain can be as large as ~3–5%, as calculated from the measured displacement in the graphene lattice. Because the PMFs are proportional to the strain level according to the relation $B_s \approx \frac{\hbar}{e} \frac{8\beta\mathcal{U}}{aD} \propto \mathcal{U}$ (where $\mathcal{U}$ is the strain, β is the electronic hopping between p_z orbitals located at nearest-neighbour atoms and a is the distance between them, D is the diameter of the strained region, $\hbar$ is reduced Planck's constant and e is the electron charge)[5,6,9], the PMFs in G–BP decrease with decreasing biaxial strain, which in turn decreases with increasing rotation angle.

Angle-dependent Raman spectroscopy confirms that the presence of strain coupling between the BP and graphene lattices is strongest (Fig. 3d) when the two lattices are aligned in their respective zigzag direction (at $\theta = 0°$) (Supplementary Fig. 10)[22–24].

Orientation-dependent interlayer interaction

To obtain an insight into the bonding interactions between graphene and BP when both lattices are aligned in the zigzag direction, we performed first-principles calculations of a graphene monolayer superimposed on a bilayer BP supercell. We used the density-functional-theory (DFT)-based Vienna ab initio simulation package (VASP5.4.4)[25] with the Perdew–Burke–Ernzerhof (PBE) format exchange-correlation functional and the projector augmented wave (PAW) potentials[26]. A unit cell containing a $(4 \times \sqrt{3})$ graphene supercell and a (3×1) bilayer BP supercell are superimposed on one another with their lattices aligned in the zigzag direction.
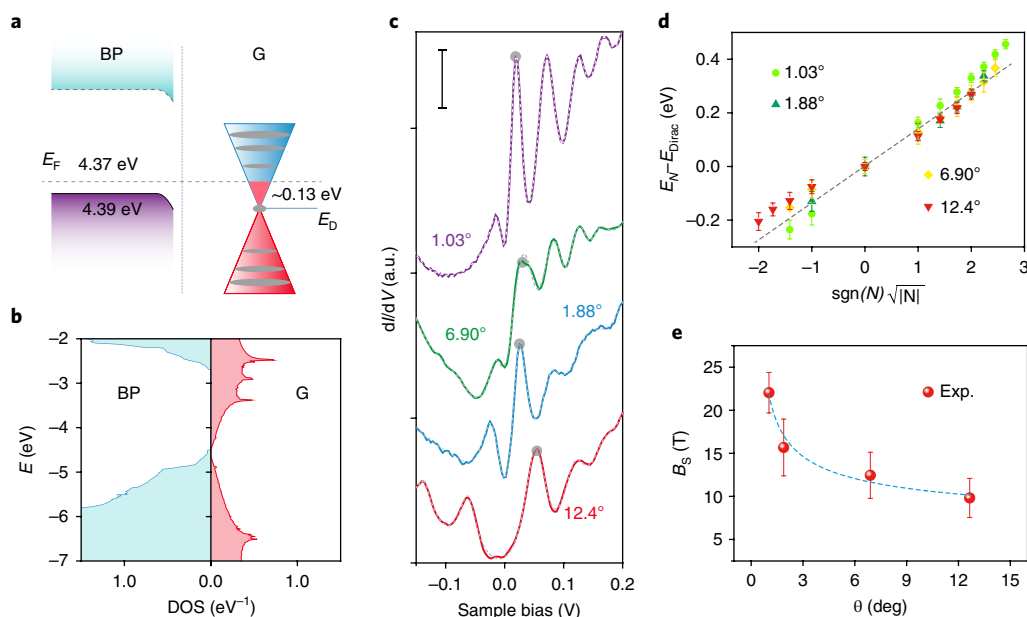
Fig. 5 | Angle-dependence of STS spectra and pseudo-magnetic fields. a, Alignment of bands of strained graphene (G) and multilayer black phosphorus (BP). The values for work function, band edge and relative doping are determined from ARPES and XPS. E_F and E_D refer to the Fermi level energy and Dirac point energy of graphene, respectively. **b**, Band structure of the heterostructure formed from strained graphene and BP; the biaxial strains applied on graphene are +0.8% along one zigzag direction and +3.0% perpendicular to this zigzag direction. For BP, the strain is −5.0% along its armchair direction and −0.6% along its zigzag direction. **c**, dI/dV spectra collected from different G–BP samples with four representative corresponding moiré patterns. The valence band of multilayer BP is close to and even buries the Dirac point of graphene, depending on the rotation angle and the doping level of the BP crystal. A series of peaks are clearly visible in the positive sample bias region. Dashed lines show fitted data using quartic background and Gaussian peaks; the spectra have been offset vertically for clarity. $N = 1$ peaks are marked with grey circles. The STS spectra were acquired at the ridge region of each moiré pattern. **d**, Scaled energy levels as a function of Landau level index. The dashed line is a guide to illustrate the linear behaviour of plots from each angle. See Supplementary Fig. 14 for linear fitting of each plots. Error bars indicate s.d. of scaled energies for each angle. **e**, Measured pseudo-magnetic field as a function of rotation angle in the G–BP system. The blue guide line shows the observed trend. Error bars represent s.d. of pseudo-magnetic fields at different angles.

According to our DFT calculations (Fig. 4a), graphene and BP are separated by a van der Waals gap of 3.5 Å. Due to the lattice mismatch, strain occurs both for BP (~0.9% along the zigzag direction and ~6% along the armchair direction) and graphene (~0.6% along the zigzag direction and ~1.2% along the armchair direction)[10,18]. As shown in Fig. 4b, the band structures of graphene and BP in the heterostructure are similar to their respective isolated counterparts. However, strongly anisotropic orbital hybridization between graphene and BP is observed: the p_z orbital hybridization is most obvious along the Γ–X direction (zigzag direction) near the Fermi level, whereas it is insignificant along the Γ–Y direction (armchair direction). This orientation-dependent interlayer interaction may play a dominant role in shear strain formation in the graphene basal plane.

Angle-dependent pseudo-Landau levels

It is known that the presence of PMFs will modify the band structure to form pseudo-Landau levels (pLLs) in strained graphene, which can be observed by scanning tunnelling spectroscopy (STS; the recorded spectrum reflects the local density of states)[8,27–29]. The energies of these pLLs with respect to the Fermi level follow the expression

$$E_N - E_{\text{Dirac}} = \text{sgn}(N)\sqrt{2e\hbar v_F^2 B_S} \times \sqrt{|N|} \qquad (2)$$

Where E_N and E_{Dirac} is the Nth Landau level energy and the Dirac point energy with respect to the Fermi level, B_S is the pseudo-magnetic field, v_F is the Fermi velocity, $\hbar$ is the reduced Planck's constant and e is the electron charge. However, when multilayer BP with

a small bandgap of ~0.31 eV is brought within the van der Waals interaction distance of graphene, the density of states (DOS) of graphene can be affected, for example, by charge transfer from BP[16,17]. Insights into the band edge alignment between graphene and BP is obtained from X-ray photoelectron spectroscopy (XPS) and angle-resolved photoemission spectroscopy (ARPES; Supplementary Fig. 11). The data show that graphene becomes slightly n-doped (~0.13 ± 0.06 eV) and its Dirac point lies at the valence band edge of multilayer BP, as shown in Fig. 5a. Figure 5b sketches the DOS and band alignment of monolayer graphene and bulk BP under a biaxial strain ranging from −5.0% to +3.0%, comparable to the observed values (see Supplementary Fig. 12 for more combinations of biaxial strain levels). The Dirac point of graphene is located ~0.1 eV above the valence band of BP, and the bandgap of strained BP is increased from 0.3 eV to >1.0 eV (Fig. 5a and Supplementary Fig. 12). The enlarged bandgap of the underlying BP means that graphene is electrically decoupled from the BP layer in the low energy range (especially when under positive sample bias).

Because a PMF induces zero external magnetic field Landau level quantization, the energies of the pLL peaks are related to the magnitude of the PMF, which is in turn related to the strain inherent in the moiré superlattice. Figure 5c shows four representative dI/dV spectra[5,8,27] acquired on each moiré superlattice. The dI/dV data taken at the four superlattice structures show that the minimum intensities appear at negative sample biases (−0.045 to −0.12 eV), a clear indication that graphene is slightly n-doped by the BP flake (see Supplementary Fig. 13 for a wider energy range STS spectra). Moreover, a series of sharp peaks with varying pLL spacings are observed in the tunnelling spectrum of all four lattices. Because the Dirac point of graphene lies very
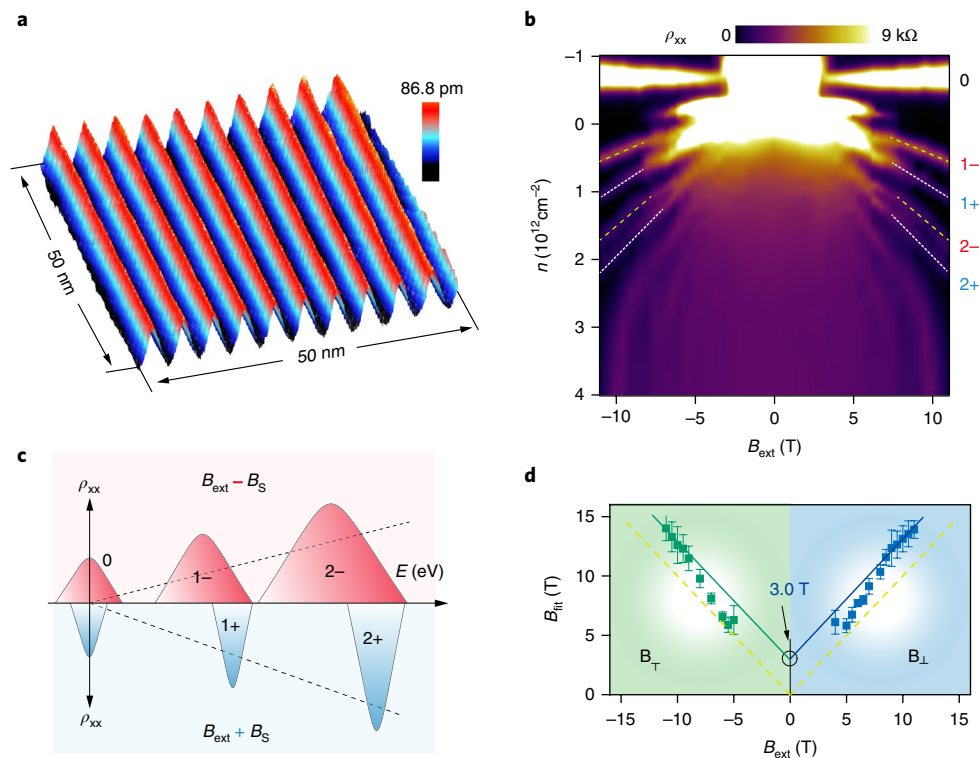
Fig. 6 | Transport data of a G–BP (thickness ~8 nm) device with Hall bar geometry. a, Three-dimensional STM topography image of G–BP heterostructure showing uniform moiré pattern on a mesoscopic scale (50 × 50 nm). The absolute amplitude of the large moiré superlattice is ~55 ± 9 pm (as shown in Supplementary Fig. 21). **b**, Landau fan diagram of longitudinal resistance ρ_{xx} (B_{ext}, n), measured at 1.5 K. B_{ext} represents the applied external magnetic fields and n is the carrier density, respectively. For graphene on a thin BP flake that is not sufficient to maintain the as-generated strain, see the Landau fan diagram and additional discussions in Supplementary Note 19 and Supplementary Fig. 20. **c**, Schematic drawing of pLLs from two valleys under an external magnetic field (B_{ext}), showing a plot of ρ_{xx} positions versus energy (E). **d**, Fitted data for estimating the pseudo-magnetic field (B_s) in a G–BP superlattice. Only the positive branch (for example, curves labelled 1+ and 2+ in **b**) was used in the analysis to determine B_{fit} because of insufficient resolution for the negative branch. The yellow dashed line (slope = 1) corresponds to the situation when $B_s = 0$ T, and blue and green regions represent results collected under perpendicular external magnetic fields along opposing directions. B_{fit} is the fitted effective magnetic field, and $B_\perp$ and $B_\top$ are the two perpendicular external magnetic fields with direction from G to BP and from BP to G, respectively. Error bars represent s.d. of the fitted pseudo-magnetic field.

close to the valence band edge of the BP flake, the pLLs near the Dirac point are broadened. To precisely identify the peak positions, the peaks were fitted to a series of Gaussians after subtracting a simple polynomial background (see fitting method in Supplementary Note 13)[8,27]. The normalized energies $E_N - E_{Dirac}$ are plotted in Fig. 5d as a function of sgn(N)$\sqrt{|N|}$ for the four superlattices. Combining the linear fitting slope of each dataset (for more details see Supplementary Note 13 and Supplementary Fig. 14) with equation (2), the values of the PMFs are estimated to be 22 ± 3 T, 16 ± 4 T, 12 ± 3 T and 10 ± 3 T for $\theta \approx 1.03°$, 1.88°, 6.9° and 12.4°, respectively. The uncertainties are the standard deviations of five measurements near the quasi-1D ridges. This points to a monotonically decreasing PMF with increasing rotation angle (Fig. 5e). This trend obtained from the pLLs sequence is consistent with the fact that a decrease in biaxial strain is expected as θ increases. Based on our calculations, any pseudo electric fields that arise from the non-uniform strain on graphene will not be large enough to destroy pLL quantization (for an extended discussion on pseudo electric fields see Supplementary Note 4 and Supplementary Figs. 5 and 6)[30,31]. We have also ruled out that these pLL peaks are due to perturbations of the local DOS of graphene by the periodic potential (for a detailed discussion see Supplementary Note 14 and Supplementary Fig. 15)[32,33].

Quantized conductance in mesoscopic samples
Figure 6a shows a STM large-area scan of the G–BP superlattices (for a 100 × 100 nm² area scan, see Supplementary Fig. 16b), dem-

onstrating that a uniform quasi-1D superlattice can be realized in mesoscopic systems. To investigate the influence of PMF on the transport properties of graphene, G–BP field-effect transistor (FET) devices in a Hall bar geometry were fabricated (Supplementary Fig. 17a, $\theta \approx 1.0 \pm 1.5°$). We have also verified that the electronic contribution from the multilayer BP substrate is minimal at low gate bias, which supports the fact that the characteristic peaks shown in Fig. 5c should originate from graphene (for measurements on a bare BP FET device with thickness ~8 nm, see Supplementary Fig. 18)[16,17].

Due to time-reversal symmetry, the strain-induced pseudo-magnetic fields have opposite directions in the K and K′ valleys of graphene. In the presence of an external magnetic field (B_{ext}), however, B_{ext} and the strain-induced B_s either add up or cancel, hence giving rise to a valley-dependent effective magnetic field (B_{eff}), which in turn creates valley polarization of the Landau levels. However, the experimental fingerprint of PMF on quantum transport, as well as on the valley Hall effect (an anomalous Hall effect whose sign depends on the valley index in two-dimensional crystals), has remained elusive so far[3,6,8,34]. With B_{ext} and PMF, the effective magnetic fields in the two valleys are given by $B_{ext} - B_s$ and $B_{ext} + B_s$ (refs [6,31]). Consequently, the valley degeneracy of the $N \neq 0$ LLs is expected to be lifted for the Nth LLs and a splitting of the two valleys should be observed. Figure 6b shows the fan diagram of the longitudinal resistance (ρ_{xx}) as a function of B_{ext} and carrier density (n). A splitting of longitudinal resistance peaks ($N = +1, +2$) could be observed (dashed lines marked as 1−, 1+, 2− and 2+) when

$B_{ext} \geq 8.0\,T$ owing to different effective magnetic fields for the two valleys. When B_{ext} is slightly larger than B_s, the effective field in one valley is additive, but it is subtractive in the other; thus, incomplete quantization is observed in the weaker field valley, which results in broadening of the ρ_{xx} peaks (1− and 2−, red peaks in Fig. 6c) and possible overlap with other LLs. For the stronger field valley ($B_{eff} = B_{ext} + B_s$), relatively sharper ρ_{xx} peaks labelled as 1+ and 2+ are clearly seen. For each pLL, the ρ_{xx} peak positions depend linearly on B_{eff} ($n = \nu e B_{eff} / h$; see Supplementary Fig. 17c for the theoretical case and Supplementary Fig. 17e for the experimental case), so, by fitting the positions of $N+\rho_{xx}$ peaks (blue peaks in Fig. 6c) against carrier density, a fitted effective magnetic field $B_{fit} = B_{eff} = B_{ext} + B_s$ can be estimated as shown in Fig. 6d[13,14,31,34]. When B_{ext} is twice as large as B_s ($B_{ext} \geq 8.0\,T$), the corresponding plot fits well to a straight line with slope of 1; extrapolating to $B_{ext} = 0$ gives $B_s \approx 3.0\,T$. This measured B_s value is an average of the spatially undulating PMF (Fig. 3b) extending over micrometre length scales, so it is lower in comparison with the $B_s \sim 10–20\,T$ estimated from local STS measurements (acquired at the top of quasi-1D ridges), which may also arise from other factors including strain relaxation along the edge, imperfect superlattices and dilution by the spatial gradient (with low PMFs) near the boundary, where the direction of PMFs changes. Nonetheless, this is the first time that the influence of PMFs has been identified in transport studies, which is different from the spatially localized effects reported previously[8,9,29,35]. It is worth mentioning that Weiss oscillations can appear in the transport measurements of graphene subjected to a periodic potential[36–39]. To rule out this possibility, both the longitudinal resistance ρ_{xx} and the transverse conductivity σ_{xy} (Supplementary Fig. 19) were recorded, and it was found that the steps in σ_{xy} (with carrier density n) are perfectly correlated with the maxima of ρ_{xx}. The σ_{xy} data show that the quantized steps at $(\pm 4N + 2)e^2 / h$ and ρ_{xx} peaks scale linearly with n (Fig. 6b) instead of $\sqrt{n}$ (Weiss oscillations scale as $\sqrt{n}$), thereby indicating that the pseudo Landau levels are due to the quantum Hall effect (QHE) and are not related to Weiss oscillations.

Conclusions

In summary, we have demonstrated a viable method to engineer large-scale PMFs on graphene by shear-straining it on multilayer BP. Furthermore, we show that the PMFs can be tuned in terms of strength and spatial distribution by the rotation angle of the graphene on the BP. Importantly, our work suggests that interfacing graphene with substrates that are mismatched in terms of symmetry and crystal lattice, allied with anisotropic van der Waals interactions, provides a strategy to generate strain texture on graphene that is intertwined with PMFs. Unlike the localized PMF previously observed on curved structures such as wrinkles or bubbles, the graphene-on-BP superlattice is planar and generates a PMF that can extend over the entire G–BP sample. It is generally believed that the observation of the quantum Hall effect in transport is not possible without the breaking of either time-reversal symmetry or pseudospin rotational symmetry[5]. At large external magnetic fields ($B_{ext} > 8T$), our observations clearly show the effect of PMFs on the Landau quantization criteria with an effective magnetic field $B_{eff} = B_{ext} + B_s$. Additional theoretical and experimental work is required to fully explore this crossover from the usual quantum Hall effect at weak time-reversal symmetry breaking to this new PMF-enhanced quantum Hall effect at strong time-reversal symmetry breaking[40]. Yet, the demonstration of PMFs over tens of micrometres brings the prospect of PMF-confined quantized conductance or valley polarized current (that is, valley filtering) in graphene a step closer.

Methods

Methods, including statements of data availability and any associated accession codes and references, are available at https://doi.org/10.1038/s41565-018-0178-z.

References

1. Novoselov, K. S. et al. A roadmap for graphene. *Nature* **490**, 192–200 (2012).
2. Castro Neto, A. H., Guinea, F., Peres, N. M. R., Novoselov, K. S. & Geim, A. K. The electronic properties of graphene. *Rev. Mod. Phys.* **81**, 109–162 (2009).
3. de Juan, F., Mañes, J. L. & Vozmediano, M. A. Gauge fields from strain in graphene. *Phys. Rev. B* **87**, 165131 (2013).
4. Vozmediano, M. A. H., Katsnelson, M. I. & Guinea, F. Gauge fields in graphene. *Phys. Rep.* **496**, 109–148 (2010).
5. Guinea, F., Katsnelson, M. I. & Geim, A. K. Energy gaps and a zero-field quantum Hall effect in graphene by strain engineering. *Nat. Phys.* **6**, 30–33 (2010).
6. Low, T. & Guinea, F. Strain-induced pseudomagnetic field for novel graphene electronics. *Nano Lett.* **10**, 3551–3554 (2010).
7. Guinea, F., Horovitz, B. & Le Doussal, P. Gauge field induced by ripples in graphene. *Phys. Rev. B* **77**, 205421 (2008).
8. Levy, N. et al. Strain-induced pseudo-magnetic fields greater than 300 tesla in graphene nanobubbles. *Science* **329**, 544–547 (2010).
9. Jiang, Y. et al. Visualizing strain-induced pseudomagnetic fields in graphene through an hBN magnifying glass. *Nano Lett.* **17**, 2839–2843 (2017).
10. Lee, C., Wei, X., Kysar, J. W. & Hone, J. Measurement of the elastic properties and intrinsic strength of monolayer graphene. *Science* **321**, 385–388 (2008).
11. Geim, A. K. & Grigorieva, I. V. Van der Waals heterostructures. *Nature* **499**, 419–425 (2013).
12. Yankowitz, M. et al. Emergence of superlattice Dirac points in graphene on hexagonal boron nitride. *Nat. Phys.* **8**, 382–386 (2012).
13. Hunt, B. et al. Massive Dirac fermions and Hofstadter butterfly in a van der Waals heterostructure. *Science* **340**, 1427–1430 (2013).
14. Dean, C. R. et al. Hofstadter's butterfly and the fractal quantum Hall effect in moiré superlattices. *Nature* **497**, 598–602 (2013).
15. Mishchenko, A. et al. Twist-controlled resonant tunnelling in graphene/boron nitride/graphene heterostructures. *Nat. Nanotech.* **9**, 808–813 (2014).
16. Xia, F., Wang, H. & Jia, Y. Rediscovering black phosphorus as an anisotropic layered material for optoelectronics and electronic. *Nat. Commun.* **5**, 4458 (2014).
17. Li, L. et al. Black phosphorus field-effect transistors. *Nat. Nanotech.* **9**, 372–377 (2014).
18. Appalakondaiah, S., Vaitheeswaran, G., Lebegue, S., Christensen, N. E. & Svane, A. Effect of van der Waals interactions on the structural and elastic properties of black phosphorus. *Phys. Rev. B* **86**, 035105 (2012).
19. Wu, J. et al. Identifying the crystalline orientation of black phosphorus using angle-resolved polarized Raman spectroscopy. *Angew. Chem. Int. Ed.* **127**, 2396–2399 (2015).
20. Pereira, V. M. & Castro Neto, A. H. Strain engineering of graphene's electronic structure. *Phys. Rev. Lett.* **103**, 046801 (2009).
21. Artaud, A. et al. Universal classification of twisted, strained and sheared graphene moiré superlattices. *Sci. Rep.* **6**, 25670 (2016).
22. Park, C.-H., Yang, L., Son, Y.-W., Cohen, M. L. & Louie, S. G. Anisotropic behaviours of massless Dirac fermions in graphene under periodic potentials. *Nat. Phys.* **4**, 213–217 (2008).
23. Yoon, D. et al. Strong polarization dependence of double-resonant Raman intensities in graphene. *Nano Lett.* **8**, 4270–4274 (2008).
24. Ferrari, A. C. & Basko, D. M. Raman spectroscopy as a versatile tool for studying the properties of graphene. *Nat. Nanotech.* **8**, 235–246 (2013).
25. Kresse, G. & Hafner, J. Ab initio molecular-dynamics simulation of the liquid-metal–amorphous-semiconductor transition in germanium. *Phys. Rev. B* **49**, 14251 (1994).
26. Perdew, J. P., Burke, K. & Ernzerhof, M. Generalized gradient approximation made simple. *Phys. Rev. Lett.* **77**, 3865 (1996).
27. Miller, D. L. et al. Observing the quantization of zero mass carriers in graphene. *Science* **324**, 924–927 (2009).
28. Li, S. Y. et al. Observation of unconventional splitting of Landau levels in strained graphene. *Phys. Rev. B* **92**, 245302 (2015).
29. Song, Y. J. et al. High-resolution tunnelling spectroscopy of a graphene quartet. *Nature* **467**, 185 (2010).
30. Gibertini, M., Tomadin, A., Polini, M., Fasolino, A. & Katsnelson, M. I. Electron density distribution and screening in rippled graphene sheets. *Phys. Rev. B* **81**, 125437 (2010).
31. Castro, E. V., Cazalilla, M. A. & Vozmediano, M. A. Raise and collapse of pseudo Landau levels in graphene. *Phys. Rev. B* **96**, 241405 (2017).
32. Slotman, G. J. et al. Effect of structural relaxation on the electronic structure of graphene on hexagonal boron nitride. *Phys. Rev. Lett.* **115**, 186801 (2015).
33. Woods, C. R. et al. Commensurate–incommensurate transition in graphene on hexagonal boron nitride. *Nat. Phys.* **10**, 451–456 (2014).

34. Müller, J. E. Effect of a nonuniform magnetic field on a two-dimensional electron gas in the ballistic regime. *Phys. Rev. Lett.* **68**, 385–388 (1992).

35. Goerbig, M. O. Electronic properties of graphene in a strong magnetic field. *Rev. Mod. Phys.* **83**, 1193 (2011).

36. Weiss, D., von Klitzing, K., Ploog, K. & Weimann, G. Magnetoresistance oscillations in a two-dimensional electron gas induced by a submicrometer periodic potential. *Europhys. Lett.* **8**, 179–184 (1989).

37. Peeters, F. M. & Vasilopoulos, P. Quantum transport of a two-dimensional electron gas in a spatially modulated magnetic field. *Phys. Rev. B* **47**, 1466 (1993).

38. Carmona, H. A. et al. Two dimensional electrons in a lateral magnetic superlattice. *Phys. Rev. Lett.* **74**, 3009 (1995).

39. Matulis, A. & Peeters, F. M. Appearance of enhanced Weiss oscillations in graphene: Theory. *Phys. Rev. B* **75**, 125429 (2007).

40. Roy, B., Hu, Z. X. & Yang, K. Theory of unconventional quantum Hall effect in strained graphene. *Phys. Rev. B* **87**, 121408 (2013).

Competing interests

The authors declare no competing interests.

Additional information

Supplementary information is available for this paper at https://doi.org/10.1038/s41565-018-0178-z.

Reprints and permissions information is available at www.nature.com/reprints.

Correspondence should be addressed to K.P.L or S.A. or J.L.

Publisher's note: Springer Nature remains neutral with regard to jurisdictional claims in published maps and institutional affiliations.

Methods

Device fabrication and characterization. The exfoliation of BP was carried out in a glove box under argon gas (O_2 and H_2O levels <0.5 ppm). Typically, a thin BP flake was mechanically exfoliated from a bulk BP crystal (HQ Graphene) onto a silicon substrate using blue 'magic' tape. Next, a BP flake of appropriate size and thickness was identified using optical microscopy. This procedure was also carried out inside the glove box to avoid degradation of the BP. For STM studies, thin BP flakes of ~20–50 μm edge size were overlaid on a silicon wafer with as-grown high-quality CVD graphene using a semi-dry method with an in-house transfer platform in an argon-filled glove box, followed by patterning with gold pads (dimensions of ~400 × 400 μm² and 50 nm thickness, thermally deposited). To prevent tip crash, care was taken to completely cover both the BP flake and the neat Si/SiO₂ substrate with chemical vapour deposited (CVD) graphene (Supplementary Fig. 22). The wiring between the gate electrode and the sample was made of Al. After wire bonding, the BP sample was annealed at 220 °C in the preparation chamber (<1 × 10⁻¹⁰ torr) to remove residual absorbents and to achieve a better contact (Supplementary Fig. 23). While fabricating G–BP heterostructures for low-temperature transport measurements, monolayer graphene was exfoliated from Kish graphite and aligned onto the BP flake with the desired rotation angle with the assistance of the transfer platform, so as to achieve uniform 1D moiré patterns over a large area. This transfer process was also carried out inside the argon-filled glove box. The thickness and morphology of the devices were verified using Dimension FastScan AFM (Bruker) in tapping mode. The orientations of the BP flake were determined by angle-resolved polarized Raman spectroscopy (Renishaw) and polarized optical microscopy[16,19]. To obtain precise control of the rotation angle, we chose graphene flakes with well-defined facets, where the crystallographic orientations can be identified by comparing the intensities of the Raman D peak acquired at the edge[15]. By controlling the angle of alignment of the zigzag edge of the graphene with respect to the zigzag direction of the BP, a G–BP heterostructure with desired rotation angle and moiré wavelength was fabricated.

STM and STS measurements. The experiments were performed in an Omicron ultrahigh-vacuum low-temperature STM (<1 × 10⁻¹¹ torr) system. The tungsten tip was calibrated by verifying the surface state of a Au (111) crystal. All the STM images were captured in constant-current mode at LN₂ and LHe temperatures. STS data were acquired using the external lock-in technique (SR830 lock-in amplifier, with bias modulations of 5–10 mV at 773.1 Hz). The gate voltage was applied using a Keithley SourceMeter (model 2400).

Low-temperature transport measurements. Electric measurements were carried out both in a ⁴He cryostat (TeslatronPT) and a physical property measurement system (PPMS) under a helium atmosphere with standard alternating-current (a.c.) lock-in amplifiers (SR830) and direct current (d.c.) techniques. Resistance versus temperature and field measurements were performed using small currents in the range 50–300 nA to avoid Joule heating. In Hall bar geometry, the channel of the G–BP device was ~1.5 μm long.

Additional characterizations. XPS, utraviolet photoelectron spectroscopy (UPS) and ARPES characterizations were implemented on bare BP and a G–BP sample to elucidate the underlying interfacial charge transfer direction between the graphene and the BP crystal. These measurements were conducted with a SPECS system (base pressure of chamber ~1 × 10⁻¹⁰ torr). The Fermi level was calibrated to Au and the binding energies of the XPS spectra were calibrated to the Au $4f_{7/2}$ peaks. XPS peak fitting was carried out using a mixed Gaussian–Lorentzian function after a Shirley background subtraction.

Theoretical calculations. See Supplementary Information for details on (1) estimation of strain tensor, pseudo electric fields and pseudo-magnetic fields; (2) first-principles calculations based on DFT to compute the electronic structure of the G–BP heterostructure, epitaxially strained bulk phosphorene and graphene, and their respective work functions; (3) estimating biaxial strain in graphene based on further extension of Hermann's formalism.

Data availability. The data that support the plots within this paper and other findings of this study are available from the corresponding authors upon reasonable request.